communications materials

A Nature Portfolio journal

Article

https://doi.org/10.1038/s43246-025-00877-1

Structural transformation for $BaBiO_{3-\delta}$ thin films grown on $SrTiO_3$-buffered Si(001) induced by an in-situ molecular beam epitaxy cooldown process

Islam Ahmed[1,2] ✉, Olivier Richard[2], Partrick Carolan[2], Marco Gambin[1,2], Luca Ceccon[1,2], Moloud Kaviani[2], Stefan De Gendt[2,3] & Clement Merckling[1,2]

Oxygen loss is a common defect type in perovskites which is caused by a low oxygen background pressure during growth. $BaBiO_{3-\delta}$ thin films are grown by molecular beam epitaxy on $SrTiO_3$-buffered Si(001) substrates. Although activated oxygen is supplied during growth, large amount of oxygen vacancies is created in the thin film depending on the cooldown process. Perovskite structure is obtained when the cooldown process includes an extended period during which activated oxygen is supplied. Another way for inducing the structural transformation is enabled via an ex-situ anneal at molecular oxygen. The transformation into $BaBiO_3$ is manifested as reconstructed octahedra based on transmission electron microscopy, Raman spectroscopy, and photoluminescence. Additionally, smaller out-of-plane lattice constant is observed for the perovskite phase supported by X-ray diffraction. Thermal mismatch and multivalency-facilitated tensile strain exerted on the layers by the underlying Si substrates are presented as the driving force behind the creation of oxygen vacancies.

Complex oxides have gained much research interest over the past few decades owing to their special properties, which enable a variety of technologies. This includes, but is not limited to, memory applications based on the ferroelectric $BaTiO_3$ and $PbTiO_3$, superconducting devices based on K-doped $BaBiO_3$ and $BaSbO_3$, and water splitting utilizing the photocatalytic activity of $NaTaO_3$[1–4]. However, the challenging part for unveiling an improved device performance lies in developing high-quality material stacks with intrinsic properties[5]. Various techniques have been widely applied for growing perovskite oxides with high quality, such as physical vapor deposition (PVD), pulsed laser deposition (PLD), sputtering, and molecular beam epitaxy (MBE). High-quality thin films with intrinsic properties have been developed by using conventional MBE, which is an important technique for the growth of perovskites with improved crystallinity and high purity. For instance, thin films of $BaSnO_3$ were reported to reach mobilities as high as those of the single crystals only when grown by MBE[6].

MBE utilizes an ultra-high vacuum environment to enable the long free path necessary for the molecular beams heading toward the substrate and for the electron beam required for in-situ reflection high-energy electron diffraction (RHEED)[7]. Upon optimizing the co-deposition parameters, the epitaxial growth proceeds in a controlled fashion thanks to the lack of high-energy species. However, one of the widely known challenges for conventional MBE is the complete oxidation of certain cations[6]. Oxygen needs to be activated to form dissociated oxygen radicals, which reach higher reactivity not possible with molecular oxygen. This is fundamentally a requirement for adsorption-controlled growth of $BaBiO_3$, where a volatile element such as bismuth has to be provided in large quantities in the presence of an aggressive oxidizing agent[8]. Applying a suitable oxidant environment can tackle the issue of the low sticking coefficient of bismuth; however, the formation of oxygen vacancies is still an issue because it also depends on the residual strain energy built up within the thin film[9]. Loss of oxygen can transform the perovskite into a sub-stoichiometric oxide, with different properties, which is common among complex oxides with a multivalent cation[10].

$SrCoO_{(3n-1)/n}$, $LaNiO_2$, and $LaCoO_{3-\delta}$ are examples of oxygen sponge materials that exhibit reversible intercalation/deintercalation of oxygen anionic planes[11–13]. Among common reasons for such occurrence of ordered oxygen vacancies are strain experienced by the thin films, growth in a reducing environment, or ionic liquid gating[14,15]. According to a density functional theory (DFT) study, $SrFeO_{2.5}$ is obtained as oxygen vacancies

[1]Department of Materials Engineering, KU Leuven, Leuven, Belgium. [2]Imec, Leuven, Belgium. [3]Department of Chemistry, KU Leuven, Leuven, Belgium.
✉e-mail: islam.ahmed@imec.be

ordered parallel to the surface under tensile strain, as this configuration maximizes the distance between the tetrahedral chains under that strain state[16]. As earlier reported, our $BaBiO_{3-\delta}$ thin films demonstrated a modulation of a BiO_4 tetrahedron every three BiO_6 octahedra due to the formation of ordered oxygen vacancy channels, resulting in an oxygen-deficient phase[17]. These ordered oxygen vacancies are formed for the as-grown thin film with an MBE recipe described in our previous work, which supplies activated oxygen radicals during the formation of the crystalline layer[8]. This structure possesses a mild breathing distortion, which is responsible for gapping the band structure[18].

In this context, the present work investigates the physical transformation occurring upon further oxidizing $BaBiO_{3-\delta}$ through different oxidative pathways. Cooldown at different activated oxygen conditions, as well as post-annealing in molecular oxygen processes, are checked for their capabilities in causing a transformation into a stoichiometric perovskite structure. The influence of the potential filling up of oxygen vacancies on the electronic structure, breathing distortion, and the optical response of the thin films is also studied. First-principles calculations were performed to gain a better understanding of the perovskite matrix's oxygen loss pathway.

Results and discussion

To investigate the effect of process control over the formation of ordered oxygen vacancies, $BaBiO_{3-\delta}$ thin films of 25 nm were epitaxially grown on Si(001) with a buffer layer of $SrTiO_3$(001). During growth, the temperature was fixed at 600 °C while supplying activated oxygen species to the growth surface with a plasma power of 600 W, at a base chamber pressure around 1E-6 Torr. Bismuth was evaporated in higher quantities compared to barium to satisfy the adsorption-controlled growth conditions[6]. During the cooldown process, three samples had either molecular oxygen (0 W), activated oxygen (200 W), or activated oxygen (600 W) supplied for 5 min, and the rest of the cooldown down process was carried out at a cleaner vacuum. For another set of samples, the plasma power remained fixed at 600 W but the time during which the activated oxygen is supplied was extended to 10, 20, or 40 min instead of only 5 min, as elucidated in Fig. 1a.

Additionally, sample A (cooled down in activated oxygen for 5 min with plasma power of 200 W) was ex-situ annealed in a molecular oxygen environment in an Annealsys AS-One 150 oven. Annealing was carried out at 600 °C at 760 Torr. The ex-situ annealing in molecular oxygen is carried out to compare the anneal step with the 40-min cooldown process at plasma power of 600 W (sample B).

The obtained layers are studied by XRD, and the results are shown in Fig. 2. Samples which were entirely cooled down in vacuum and partly in molecular oxygen have amorphous layers with no diffraction. For the 5-min cooldown process with activated oxygen at 200 W and 600 W, both layers have an out-of-plane lattice constant of 4.36 Å. Another interesting observation is that as the time during which the surface is provided with activated oxygen at 600 W increases, the out-of-plane lattice constant shrinks, as clarified in Table 1. This effect is observed only for $BaBiO_{3-\delta}$ layers, while the out-of-plane lattice constant for $SrTiO_3$ remains unchanged at 3.91 Å.

Figure 3a, d shows the time evolution of RHEED patterns along the <100> crystallographic directions during the first 120 s of the growth with a step of 20 s as well as the RHEED patterns after cooling down for sample A (5 min/200 W) and sample B (40 min/600 W), respectively. It is noticed that the in-plane lattice constant does not evolve with time since the beginning of the growth as compared to that at the surface of the 25 nm thin films after cooling down. This confirms that both sample A and sample B have domain matching epitaxy as the mechanism for the growth of $BaBiO_{3-\delta}$ on $SrTiO_3$, given the large lattice mismatch ($f \approx 11.77\%$), where 8 unit cells of $BaBiO_{3-\delta}$ are accommodated on 9 unit cells of $SrTiO_3$ as illustrated in our previous TEM study[17]. Despite the difficulty in obtaining images of low noise levels due to the fragility of this material upon e-beam exposure[19], TEM still gives important insights about the crystal structure. In the TEM images in Fig. 3b, c, it is obvious that the cooldown for 5 min at 200 W of oxygen plasma results in a layer of $BaBiO_{3-\delta}$ with ordered oxygen vacancies, as observed based on the darker contrast areas aligned parallel to the substrate surface. Upon extending the time, during which activated oxygen is supplied at a higher plasma power of 600 W, to 40 min, the oxygen vacancies are sufficiently filled up to retrieve the perovskite structure.

Monoclinic charge ordering is a characteristic property for $BaBiO_3$, which results in the occurrence of breathing lattice distortion due to the double valency on the bismuth ionic sites (Bi^{3+} & Bi^{5+}). The breathing distortion on the BiO_6 octahedra is manifested in the layer as a Raman spectral response at 565 cm^{-1}. According to Fig. 4a, there is a correlation between the lattice constants of the layers and the Raman spectral intensity. The highest intensity response is recorded when activated oxygen is provided for 40 min during the cooldown process, which results in the smallest out-of-plane lattice constant layer (perovskite structure). This distortion is fundamentally responsible for opening a Peierl's gap in the band structure of around 2.07 eV, according to a DFT study[20]. Therefore, the influence of the cooldown process on the PL is like that observed for the Raman spectra. The layers go from a mild optical response at 2.19 eV when ordered oxygen vacancies exist in the structure to a more pronounced response when the perovskite structure is retrieved. While no response is recorded for the amorphous layers, as expected.

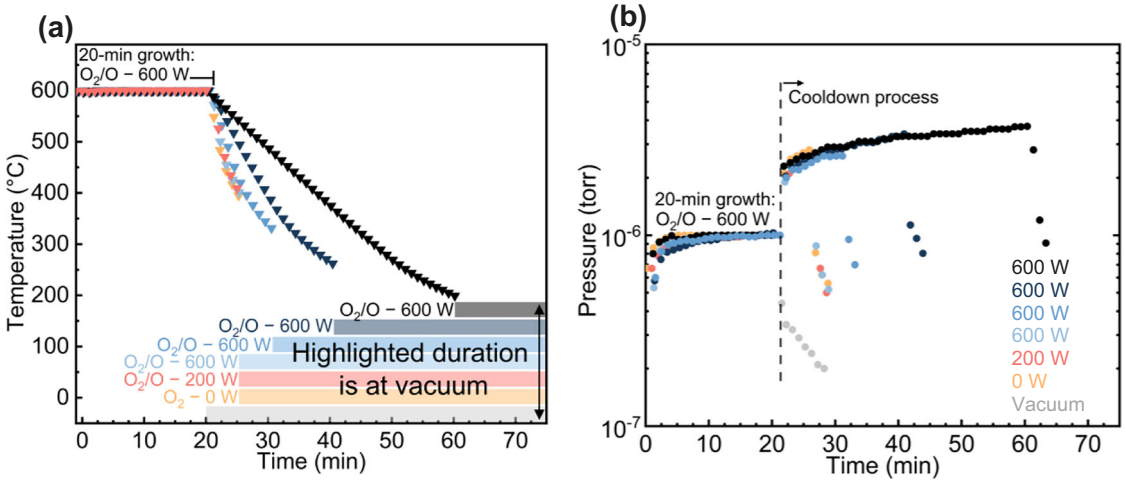

Fig. 1 | Representation of the growth and cooldown conditions. a Temperature in a function of time for the growth process of 20 min and the cooldown process for the different samples at different oxygen conditions, as stated next to the colored bars. Colored bars represent the time during which the cooldown is carried out in a vacuum. **b** Pressure data as a function of time for both the growth and cooldown processes for the different samples.

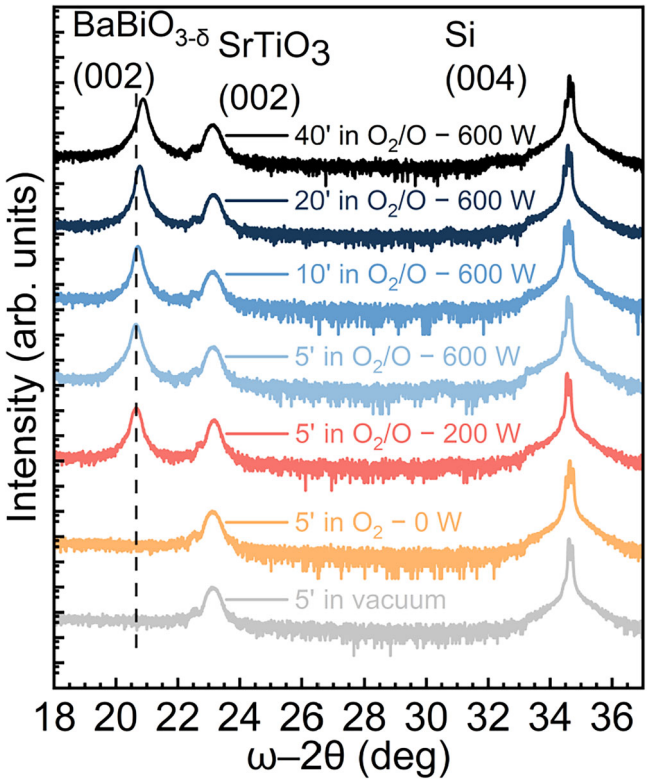

Fig. 2 | Crystallinity assessment for the different cooldown conditions. XRD's out-of-plane symmetric scans showing diffraction from Si substrates' (004), $SrTiO_3$ buffer layers' (002), and $BaBiO_{3-\delta}$ active layers' (002) planes. XRD data highlights the effect of both the oxidative environment during the cooldown process as well as the time during which activated oxygen is supplied at 600 W.

Table 1 | Lattice parameters of $BaBiO_{3-\delta}$ as a result of varying the cooldown time

Cooling time (min)	c (Å)
5.0	4.36
10.0	4.35
20.0	4.34
40.0	4.32

Results presented so far are based on the in-situ cooldown process in the MBE chamber. However, the ex-situ anneal process at molecular oxygen is also discussed in this study. Interestingly, as presented in Supplementary Fig. S1a, the annealing process at molecular oxygen results in a reduction in the out-of-plane lattice constant of 1% for sample A (going from 4.36 Å down to 4.32 Å). Upon comparison with sample B, the ex-situ anneal for 5 min at 600 °C in an atmospheric pressure molecular oxygen environment has the same effect on the layer. The reduction in the out-of-plane lattice constant for $BaBiO_{3-\delta}$ is accompanied by approximately a 30% increase in the layers' quality according to the FWHM of the RC, as demonstrated in Supplementary Fig. S1b. Ex-situ anneal process also results in an enhancement in the breathing distortion and the optical response, according to Supplementary Fig. S2b, c, due to the transformation into the perovskite structure with higher octahedral content.

To further evaluate the crystal structure, RSMs are collected for sample A, sample B, and sample A after the ex-situ anneal process. The RSMs reported in Fig. 5 show the (103) reflections from $BaBiO_{3-\delta}$ and $SrTiO_3$ thin films. ($\mathbf{Q_x}$ & $\mathbf{Q_z}$) axes are normalized based on $SrTiO_3$ lattice parameters. The scattering vector components $\mathbf{Q_x}$ and $\mathbf{Q_z}$ were calculated and plotted using MATLAB, according to the geometric definition $\mathbf{Q} = \mathbf{k_{out}} - \mathbf{k_{in}}$,

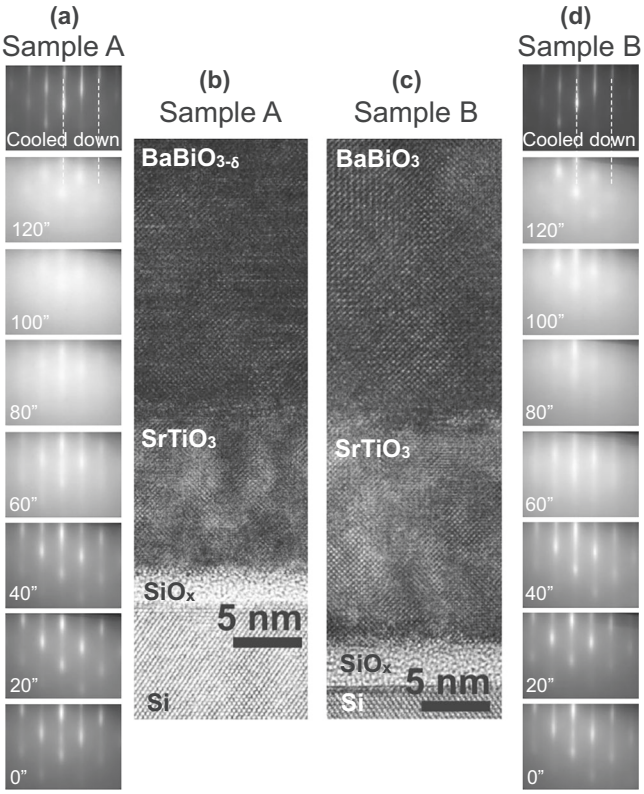

Fig. 3 | Transformation from $BaBiO_{3-\delta}$ to $BaBiO_3$. a and **d** show the time evolution of the RHEED patterns along [100] crystallographic direction during the first 120 s of the growth as well as after cooling down of the thin film for sample A and sample B, respectively. White dashed lines are drawn vertically for reference. **b** and **c** illustrate TEM images of the heterostructures: 25-nm-$BaBiO_{3-\delta}$/15-nm-$SrTiO_3$/Si(001) and 25-nm-$BaBiO_3$/10-nm-$SrTiO_3$/Si(001), respectively, with a 5-nm-long scale bar.

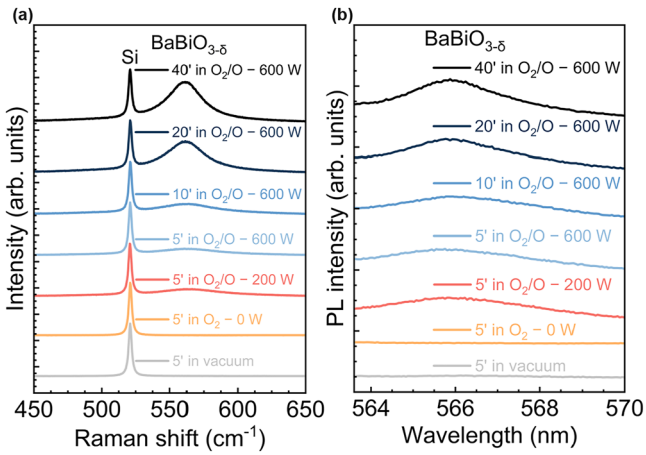

Fig. 4 | Evolution of breathing distortion and optical band gap. a Raman spectra (λ = 633 nm) normalized based on Si active mode at 521 cm^{-1}, and **b** PL spectra (λ = 532 nm), showing the response for $BaBiO_{3-\delta}$ at 2.19 eV. Both measurements were carried out at room temperature for all the different samples.

where $\mathbf{k_{out}}$ and $\mathbf{k_{in}}$ are the diffracted and incident wavevectors, respectively. Additionally, the scattering vectors in terms of real lattice vectors for a monoclinic cell are represented as: $\mathbf{Q_x} = \frac{\mathbf{k}}{\mathbf{a}}$, $\mathbf{Q_z} = \frac{\mathbf{l}}{\mathbf{c}.\sin(\beta)}$. The information provided by the out-of-plane scattering vector (Q_z) component has contributions both from the out-of-plane lattice constant (c) and the angle between the c-axis and the ab-plane (β). Indeed, evaluating β is important for $BaBiO_{3-\delta}$ since the material's monoclinicity is closely attributed to the

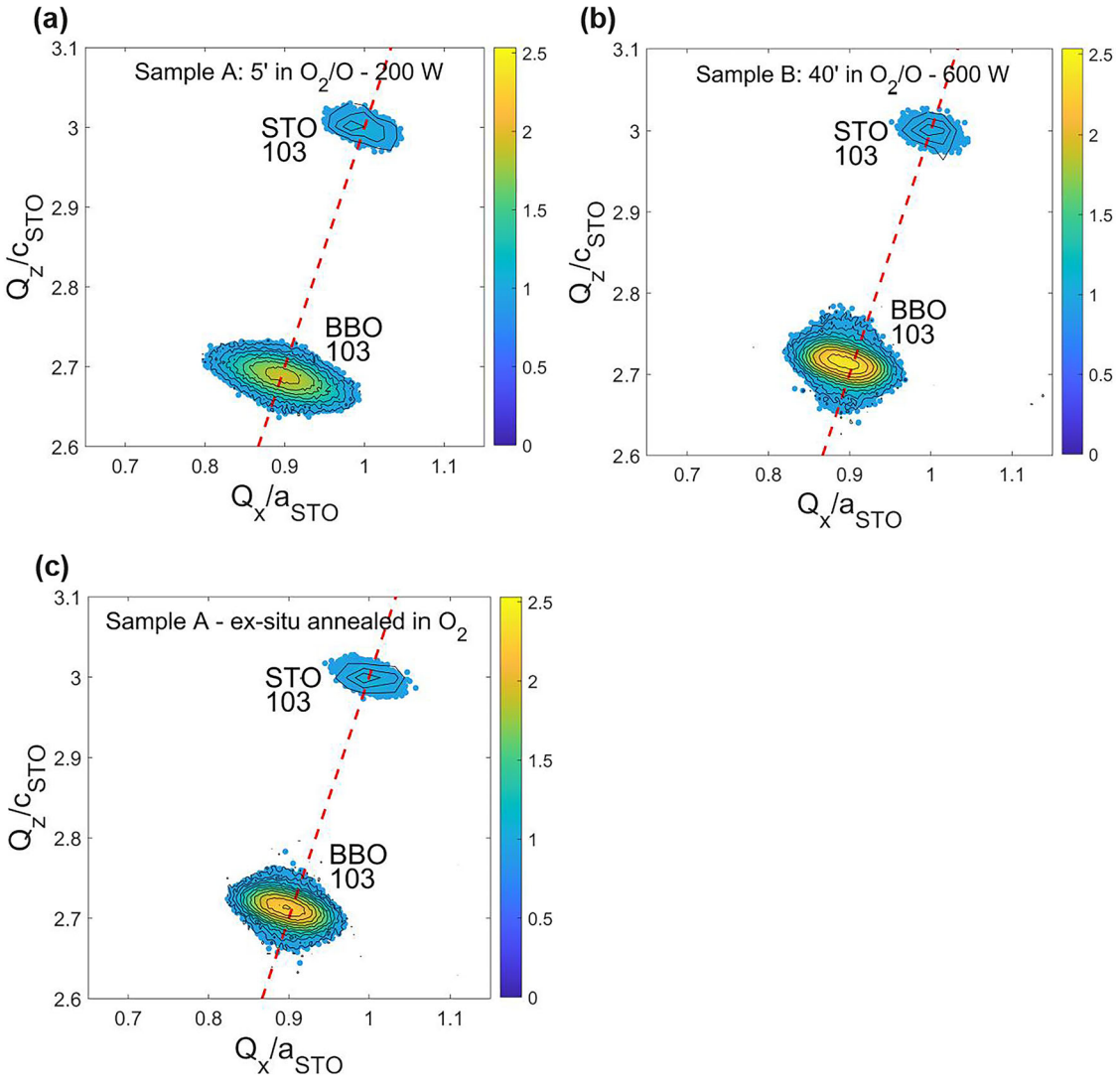

Fig. 5 | Evaluation of the lattice parameters at different process conditions. RSMs around $BaBiO_{3-\delta}$ (103) and $SrTiO_3$ (103) reflections for. **a** sample A, **b** sample B, and **c** sample A –ex-situ annealed in a molecular oxygen environment at 600 °C. Red dashed line is plotted to show the degree of deviation of the BBO structure as compared to that of STO.

spectroscopic data via the breathing distortion. To evaluate the two parameters separately, additional measurements were conducted, and a mathematical procedure described in subsection C in the supplementary information was developed. Based on the identified position of the $BaBiO_{3-\delta}$'s (103) peaks in the RSMs, the in-plane, out-of-plane, and β parameters of the cells for the different samples are evaluated and tabulated in Table 2.

For the three samples, the RSMs show totally relaxed $BaBiO_{3-\delta}$ layers with respect to $SrTiO_3$, confirming the presence of domain-matching epitaxy. Sample A has lattice parameters closest to a cubic structure with $\beta = 89.5°$. The result of both the long cooldown process at 600 W and the ex-situ anneal is manifested as two effects: contraction in the out-of-plane lattice constant by 1% and an increased monoclinicity with $\beta = 93.3°\&92.1°$ for sample B & sample A after the ex-situ anneal step, respectively.

$BaBiO_{3-\delta}$ is observed for the first time in thin film form; however, it was observed in the past in bulk form and enabled an intensive topic of research, as researchers were investigating it as a candidate material for selective oxidation catalysis[21,22]. Based on thermogravimetric experiments, at a fixed partial pressure and as a function of increasing temperatures, three distinct regions were established for $BaBiO_{3-\delta}$: $0 \le \delta \le 0.03$, $0.13 \le \delta \le 0.27$, and $0.42 \le \delta \le 0.45$, where expansion of the lattice constant upon oxygen loss was also observed[22]. The mechanism for the loss of oxygen for the thin films has not been investigated yet. However, it is possibly related to the thermal mismatch between the Si substrate and the $BaBiO_{3-\delta}$ thin film. A way to release the strain energy built up in the thin film upon cooling down rapidly could be via losing oxygen to the vacuum in an ordered fashion.

Due to the large lattice mismatch (11.77%), immediate misfit dislocation formation takes place at the earliest stage of epitaxy, which is confirmed by the delay in the RHEED streaky diffraction pattern formation, in Fig. 3a, d, as the growth starts. For domain matching epitaxy, due to the large lattice mismatches, misfit strain does not play a major role in the accumulated residual strain. The grown thin films are fully relaxed at the high growth temperature, sustaining their unstrained bulk lattice parameters[23]. As the thin film cools down, thermal strain has a major effective role in the relaxation process, in case there exists a thermal mismatch between the layer and the underlying substrate[24]. In our case, as Si has a thermal expansion coefficient of 2.6×10^{-6} °C^{-1}, while that of $BaBiO_{3-\delta}$ is 1×10^{-5} °C^{-1} (74% thermal mismatch), a tensile strain is built up within the thin film as it cools down from elevated temperature.

Tensile strain's relationship to the formation of oxygen vacancies is known for perovskite oxides; even with a small amount of tensile strain, the oxygen vacancy formation barrier is significantly lowered by reducing the efficiency of oxygen intercalation[25–27]. Additionally, tensile strain on

Table 2 | Lattice parameters of $BaBiO_{3-\delta}$ based on the RSMs for different samples: sample A, sample B, and sample A after ex-situ anneal process

	a (Å)	*b* (Å)	*c* (Å)	*β* (°)
Sample A	4.38	4.36	4.36	89.5
Sample B	4.40	4.36	4.32	93.3
Sample A – annealed	4.38	4.35	4.32	92.1

$CaFeO_{2.5}$ stabilizes the formation of ordered oxygen vacancies parallel to the substrate surface[9]. In another reduction reaction ($CaFeO_{2.5}$ to $CaFeO_2$), ordered oxygen vacancies are arranged perpendicularly regardless of the strain state of the thin film[9]. As reported in a DFT work, tensile strain not only results in increased bond length and octahedral rotation but also induces oxygen vacancy ordering because of the anisotropy of the energy of vacancy formation[28].

Stoichiometric $Ba_2Bi^{3+}Bi^{5+}O_6$ normally has an equivalent amount of Bi^{3+} and Bi^{5+}, which results in the monoclinic charge ordering. Studying the oxidation state of bismuth cations experimentally is important, as it is the reason behind the monoclinic charge ordering. XPS measurements were carried out to have a closer look at the bismuth core levels for sample A, sample B, and sample A after the ex-situ anneal process. Supplementary Fig. S2a displays the core-level spectra for bismuth for the three different samples, fitted by the two doublets, while each doublet accounts for an electronic angular momentum: $4f_{5/2}$ and $4f_{7/2}$ (with a 5.3 eV shift). All samples possess Bi^{3+} and Bi^{5+} oxidation states with an energy separation between the two peaks of around 0.75 eV. However, with careful data fitting, it turns out that the ratio Bi^{5+}/Bi^{3+} is different when comparing one sample with another. Bi^{5+}/Bi^{3+} goes from 0.95 for sample A to 1.17 after annealing the sample in high oxygen pressure. Indeed, this could be associated with the bismuth ions' environments being different according to the presence or absence of oxygen vacancy channels, which accordingly change the ionic coordination from tetrahedral to octahedral, respectively. The occurrence of oxygen vacancies triggers an imbalance of charge neutrality within the thin film, as each vacancy releases a charge of +2 ($V^{\bullet\bullet}_O$). Due to the multivalent nature of Bi ions, the thin film of $BaBiO_{3-\delta}$ can accommodate oxygen vacancies with high concentrations, in an ordered fashion, via what is so-called automatic charge neutralization. This strengthens the relationship between the strain state and the creation of ordered oxygen vacancies, similarly to perovskites containing transition metal ions[28].

As pointed out previously, according to the XRD data, this filling up of oxygen vacancies process is accompanied by a reduction in the out-of-plane lattice parameter and increased monoclinicity. This shrinkage is due to the reduced coulombic repulsion between the neighboring cations when oxygen vacancies are filled[29]. Additionally, Bi^{3+} ions are oxidized into Bi^{5+} ions, which have smaller ionic radii (Bi^{3+}—O → 2.28 Å & Bi^{5+}—O → 2.12 Å)[30]. The increased monoclinicity is in place because, as ordered oxygen vacancies are gotten rid of, the material retains its original structure, which has an expected higher monoclinic charge ordering, as the octahedra are reconstructed.

Formation energies of the bulk oxygen vacancies at different concentrations ranging from 2% up to 14% in $BaBiO_3$ with c2/m crystal symmetry were evaluated by DFT calculations and presented in Fig. 6a. Formation energies of oxygen vacancies in $BaBiO_3$ seem to be increasing as the defect concentration increases in the structure. An energy barrier of around 2.20 eV is calculated for $BaBiO_{3-\delta}$ with $\delta \approx 0.07$. This low energy of formation contributes alongside with the low oxidative environment at the MBE chamber to the spontaneous occurrence of ordered oxygen vacancies. Additionally, the formation energies of oxygen vacancies close to the terminated surface of a 40-atom slab are compared to those deeper into the layer. In Fig. 6b, it can be observed that the formation energy of a vacancy at the surface is lower than its formation deeper into the film (with an energy barrier of around 1.5 eV). This indicates that oxygen vacancies are more likely to form at the surface region or migrate there if oxygen mobility is sufficiently high, which drives the diffusion of the vacancies to the surface layer. This result leads to the formulation of a plausible pathway for the oxygen vacancy formation.

This pathway is described as follows: at such a low oxidative environment during the cooldown process: Bi—O bonds are broken; oxygen ions diffuse to the surface and combine there as oxygen molecules, which are released to the vacuum. This happens when the samples have a limited period during which activated oxygen is provided during the cooldown process. As observed in Fig. 1b, the pressure built up during 5 min for sample A quickly drops to below the pressure attained during the growth (below 1E-6 torr). However, when the cooldown process includes an extended period during which activated oxygen is provided (sample B), the pressure built up is well maintained and even increases (up to 4E-6 torr) until the sample is cooled down already well below 200 °C. This process seems to create an energy barrier for the formation of the oxygen vacancies within the film. This is, however, not the case for the sample, which is cooled down entirely in a vacuum or partly in a molecular oxygen environment, that's the reason why the crystallinity is lost soon after the samples are completely cooled down.

Conclusion

In summary, we throw light on the importance of the MBE in-situ cooldown process in regards of the oxygen vacancies formation in bismuthate perovskites. When the limited duration of supplying activated oxygen during the cooldown process is used, the thin film contains a large amount of oxygen vacancies. As domain matching epitaxy is in place, the thermal strain largely constitutes the residual strain built up during the cooldown process, especially with the 74% thermal mismatch between $BaBiO_3$ and Si. The relaxation process for this tensile strain tends to take place in the form of oxygen loss in perovskite oxides, mainly in the presence of double-valent cations, which is the case for $BaBiO_{3-\delta}$ with Bi^{3+} & Bi^{5+}. Perovskite structure is still obtainable, though by elongating the duration of supplying activated oxygen during the cooldown process or via an ex-situ anneal step an atmospheric pressure environment of molecular oxygen. Structural transformation from $BaBiO_{3-\delta}$ into $BaBiO_3$ is validated by XRD data, which show a reduction in the out-of-plane lattice constant and increased monoclinicity, as expected for $BaBiO_3$. The progressive correlation between the decrease in the out-of-plane lattice constant and the increase in the octahedral content based on the measured breathing distortion Raman signature suggests a quantitative oxygen vacancy filling up via controlling the in-situ cooldown process. Fluorine-alloyed $BaBiO_{3-\delta}$ has gained research value as a material system because of the predicted topological insulating behavior, according to DFT, and the consequent development of Majorana-fermion-based devices in case experimentally realized[31]. Regulating oxygen vacancy formation is a crucial step, as it will enable the incorporation of fluorine on the oxygen site in a well-controlled manner[32].

Methods

Growth mode and film morphology were monitored in real time by in-situ RHEED diagnostics with an electron gun operating at 20 kV. Crystalline structure of the thin films was assessed using a Phillips X'Pert Panalytical high-resolution X-ray diffraction (HR-XRD) setup, equipped with Cu-K_α radiation of 1.54 Å wavelength. Evaluating the full width at half-maximum (FWHM) of the rocking curve (RC) measurements allows for assessing the layers' crystalline quality. Reciprocal space maps (RSM) were also collected to gain a better understanding of the crystal structure and the possible strain field experienced by the layers. The crystalline structure was also evaluated based on transmission electron microscopy (TEM) images. A Titan tool with a 200 kV operating voltage was used, with a very low electron beam intensity to minimize the material damage as much as possible. For quantifying the known breathing distortion in the thin films, Raman spectroscopy was utilized with a laser of 633 nm wavelength in backscattering configuration on a Horiba Jobin-Yvon LabRAM HR800 tool. The optical band gap was investigated by the photoluminescence (PL) responses, which were collected at room temperature utilizing the same Raman tool. X-ray

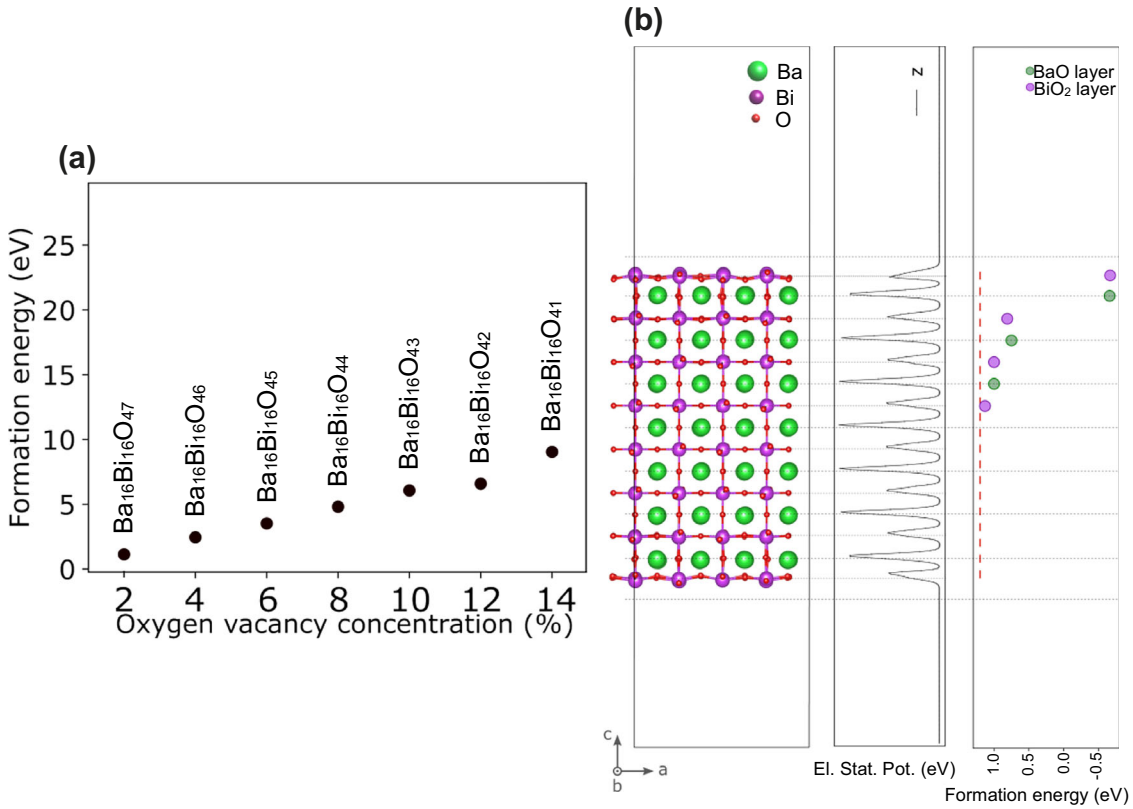

Fig. 6 | Oxygen vacancy formation and pathway. DFT calculations showing **a** formation energies at different defect concentrations for $BaBiO_3$ bulk, **b** evolution of the formation energies of V_0 at the surface of the slab compared to deeper into the film (red dashed line represents the formation energy of the bulk at this concentration).

photoemission spectroscopy (XPS) for the samples is carried out using monochromatized Al $K_{\alpha 1}$ radiation with a beam energy of 1486.6 eV, in the angle-integrated mode using a Physical Electronics Quantes instrument.

DFT calculations were performed utilizing the widely known CP2K software packages, which take into account the mixing of a Gaussian basis set with an auxiliary plane-wave basis set to solve the Kohn–Sham equations[33,34]. The DZVP-MOLOPT-SR basis sets were employed on barium, bismuth, and oxygen atoms in conjunction with the GTH pseudopotential[35,36]. The plane-wave cutoff was set to 900 Ry, which guarantees a convergence on the total energy. Additionally, to avoid the bond length overestimation typical for GGA functionals, the PBEsol exchange-correlation functional was used instead, which is known for resulting in lattice constants with a relatively higher accuracy compared to the PBE functional[37,38]. $BaBiO_{3-\delta}$ cell was constructed from the fully relaxed structure as a BiO_2-terminated 40-atom supercell.

Data availability

The data that support the findings of this study are available from the corresponding author upon reasonable request.

Received: 4 February 2025; Accepted: 1 July 2025;
Published online: 20 August 2025

References

1. Trithaveesak, O., Schubert, J. & Buchal, C. Ferroelectric properties of epitaxial $BaTiO_3$ thin films and heterostructures on different substrates. *J. Appl. Phys.* **98**, 11 (2005).
2. Venkatesan, S. et al. Monodomain strained ferroelectric $PbTiO_3$ thin films: Phase transition and critical thickness study. *Phys. Rev. B* **78**, 104112 (2008).
3. Kim, M. et al. Superconductivity in (Ba, K)SbO_3. *Nat. Mater.* **21**, 627–633 (2022).
4. Huerta-Flores, A. M. et al. Laser assisted chemical vapor deposition of nanostructured $NaTaO_3$ and $SrTiO_3$ thin films for efficient photocatalytic hydrogen evolution. *Fuel* **197**, 174–185 (2017).
5. Schlom, D. G. Perspective: Oxide molecular-beam epitaxy rocks!. *APL Mater.* **3**, 6 (2015).
6. Nunn, W., Tristan K. T., and Jalan B. A review of molecular-beam epitaxy of wide bandgap complex oxide semiconductors. *J. Mater. Res.* 1–19 (2021).
7. Schlom, D. G. et al. Oxide nano-engineering using MBE. *Mater. Sci. Eng. B* **87**, 282–291 (2001).
8. Ahmed, I., De Gendt, S. & Merckling, C. Self-regulating plasma-assisted growth of epitaxial $BaBiO_3$ thin-film on $SrTiO_3$-buffered Si (001) substrate. *J. Appl. Phys.* **132**, 22 (2022).
9. Inoue, S. et al. Anisotropic oxygen diffusion at low temperature in perovskite-structure iron oxides. *Nat. Chem.* **2**, 213–217 (2010).
10. Khare, A. et al. Topotactic metal–insulator transition in epitaxial $SrFeO_x$ thin films. *Adv. Mater.* **29**, 1606566 (2017).
11. Karvonen, L. et al. The n = 3 member of the $SrCoO_{(3n-1)/n}$ series of layered oxygen-defect perovskites. *Mater. Res. Bull.* **46**, 1340–1345 (2011).
12. Kawai, M. et al. Reversible changes of epitaxial thin films from perovskite $LaNiO_3$ to infinite-layer structure $LaNiO_2$. *Appl. Phys. Lett.* **94**, 8 (2009).
13. Biškup, N. et al. Insulating ferromagnetic $LaCoO_{3-\delta}$ films: a phase induced by ordering of oxygen vacancies. *Phys. Rev. Lett.* **112**, 087202 (2014).
14. Petrie, J. R. et al. Enhancing perovskite electrocatalysis through strain tuning of the oxygen deficiency. *J. Am. Chem. Soc.* **138**, 7252–7255 (2016).
15. Han, H. et al. Control of oxygen vacancy ordering in brownmillerite thin films via ionic liquid gating. *ACS Nano* **16**, 6206–6214 (2022).

16. Young, J. & James, M. R. Crystal structure and electronic properties of bulk and thin film brownmillerite oxides. *Phys. Rev. B* **92**, 174111 (2015).
17. Ahmed, I. et al. Influence of thickness scaling on the electronic structure and optical properties of oxygen deficient $BaBiO_{3-\delta}$ thin films grown on $SrTiO_3$-buffered Si (001) substrate. *APL Mater.* **12**, 3 (2024).
18. Lee, H. G. et al. Anisotropic suppression of octahedral breathing distortion with the fully strained $BaBiO_3/BaCeO_3$ heterointerface. *APL Mater.* **6**, 1 (2018).
19. Harris, D. T. et al. Charge density wave modulation in superconducting BaPb $O_3/BaBiO_3$ superlattices. *Phys. Rev. B* **101**, 064509 (2020).
20. Franchini, C. et al. Structural, vibrational, and quasiparticle properties of the Peierls semiconductor $BaBiO_3$: A hybrid functional and self-consistent GW+ vertex-corrections study. *Phys. Rev. B Condens. Matter Mater. Phys.* **81**, 085213 (2010).
21. Lightfoot, P. et al. $BaBiO_{2.5}$, a new bismuth oxide with a layered structure. *J. Solid State Chem.* **92**, 473–479 (1991).
22. Beyerlein, R. A., Jacobson, A. J. & Yacullo, L. N. Preparation and characterization of oxygen deficient perovskites, $BaBiO_{3-x}$. *Mater. Res. Bull.* **20**, 877–886 (1985).
23. Delhaye, G. et al. Structural properties of epitaxial $SrTiO_3$ thin films grown by molecular beam epitaxy on Si (001). *J. Appl. Phys.* **100**, 12 (2006).
24. Rasic, D. et al. "Structure-property correlations in thermally processed epitaxial LSMO films.". *Acta Mater.* **163**, 189–198 (2019).
25. Hu, S. et al. Strain-enhanced oxygen dynamics and redox reversibility in topotactic $SrCoO_{3-\delta}$ ($0<\delta\leq 0.5$). *Chem. Mater.* **29**, 708–717 (2017).
26. Petrie, J. R. et al. Strain control of oxygen vacancies in epitaxial strontium cobaltite films. *Adv. Funct. Mater.* **26**, 1564–1570 (2016).
27. Inkinen, S., Yao, L. & van Dijken, S. Reversible thermal strain control of oxygen vacancy ordering in an epitaxial $La_{0.5}Sr_{0.5}CoO_{3-\delta}$ film. *Phys. Rev. Mater.* **4**, 046002 (2020).
28. Aschauer, U. et al. Strain-controlled oxygen vacancy formation and ordering in $CaMnO_3$. *Phys. Rev. B* **88**, 054111 (2013).
29. Ullmann, H. & Trofimenko, N. Estimation of effective ionic radii in highly defective perovskite-type oxides from experimental data. *J. Alloy. Compd.* **316**, 153–158 (2001).
30. Cox, D. E. & Sleight, A. W. "Crystal structure of $Ba_2Bi^{3+}Bi^{5+}O_6$. *Solid State Commun.* **19**, 969–973 (1976).
31. Yan, B., Jansen, M. & Felser, C. A large-energy-gap oxide topological insulator based on the superconductor $BaBiO_3$. *Nat. Phys.* **9**, 709–711 (2013).
32. Yang, J. et al. The role of F-doping and oxygen vacancies on the superconductivity in SmFeAsO compounds. *Supercond. Sci. Technol.* **22**, 025004 (2008).
33. Hutter, J. et al. cp2k: atomistic simulations of condensed matter systems. *Wiley Interdiscip. Rev. Comput. Mol. Sci.* **4**, 15–25 (2014).
34. Lippert, B. G. & Parrinello, J. H. M. A hybrid Gaussian and plane wave density functional scheme. *Mol. Phys.* **92**, 477–488 (1997).
35. VandeVondele, J. & Hutter, J. Gaussian basis sets for accurate calculations on molecular systems in gas and condensed phases. *J. Chem. Phys.* **127**, 11 (2007).
36. Goedecker, S., Teter, M. & Hutter, J. Separable dual-space Gaussian pseudopotentials. *Phys. Rev. B* **54**, 1703 (1996).
37. Perdew, J. P. et al. Restoring the density-gradient expansion for exchange in solids and surfaces. *Phys. Rev. Lett.* **100**, 136406 (2008).
38. Perdew, J. P., Burke, K. & Ernzerhof, M. Generalized gradient approximation made simple. *Phys. Rev. Lett.* **77**, 3865 (1996).

Acknowledgements

This work is part of IMEC's Industrial Affiliation Program. The authors would like to thank process and hardware engineers Hans Costermans and Kevin Dubois for their dedicated support on the MBE cluster tool. The authors express their gratitude to Stefanie Sergeant, Thomas Nuytten for Raman spectroscopy measurements and analysis, and to Ilse Hoflijk, Thierry Conard for XPS measurements and analysis. This work has received funding from the European Research Council (ERC) under the European Union's Horizon 2020 research and innovation program (grant agreement No 864483).

Author contributions

Islam Ahmed: design and execution of experiments, and manuscript writing. Olivier Richard and Patrick Carolan: TEM image acquisition and sample preparation for TEM. Marco Gambin: XRD's RSM data acquisition. Luca Ceccon: ex-situ annealing processing. Moloud Kaviani: DFT calculations execution. Stefan De Gendt: supervision and manuscript revision. Clement Merckling: fund acquisition, supervision, project management.

Competing interests

The authors declare no competing interests.

Ethical approval

Local researchers had been part of the entire research process. Research was approved to be relevant by local partners. All responsibilities were agreed upon throughout the research process, on a non-discriminatory basis. No biological materials or animals were part of this research. Relevant regional and local research was cited.

Additional information

Supplementary information The online version contains supplementary material available at https://doi.org/10.1038/s43246-025-00877-1.

Correspondence and requests for materials should be addressed to Islam Ahmed.

Peer review information *Communications Materials* thanks Sajid Husain and the other anonymous reviewer(s) for their contribution to the peer review of this work. Primary Handling Editors: Zakaria Al Balushi and Aldo Isidori.